applied sciences

MDPI

Article

Dispersion Analysis of Periodically Loaded Transmission Lines with Twist Symmetry Using the Mode-Matching Technique

Oskar Zetterstrom [1,*], Guido Valerio [2], Francisco Mesa [3], Fatemeh Ghasemifard [1], Martin Norgren [1] and Oscar Quevedo-Teruel [1]

1 Division for Electromagnetic Engineering, KTH Royal Institute of Technology, 114 28 Stockholm, Sweden; fatemeh.ghasemifard@ericsson.com (F.G.); mnorgren@kth.se (M.N.); oscarqt@kth.se (O.Q.-T.)
2 Sorbonne Université, CNRS, Laboratoire de Génie Electrique et Electronique de Paris, 75252 Paris, France; guido.valerio@sorbonne-universite.fr
3 Departamento de Física Aplicada 1, E.T.S. de Ingeniería Informática, University of Seville, 4, 41004 Seville, Spain; mesa@us.es
* Correspondence: oskarz@kth.se

Received: 31 July 2020; Accepted: 23 August 2020; Published: 29 August 2020

Abstract: A mode-matching formulation is presented and used to analyze the dispersion properties of twist-symmetric transmission lines. The structures are coaxial lines periodically loaded with infinitely thin screens, which are rotated with respect to each other to possess twist symmetry. The results obtained using the proposed formulation are in good agreement with those of commercial simulators. Furthermore, using the presented mode-matching formulation, it is demonstrated that the propagation characteristics in the twist-symmetric structures are linked to the scattering and coupling of the higher order modes. The physical insight offered by this analysis is valuable for the design of various electromagnetic devices, such as filters, antennas, and phase-shifters.

Keywords: higher symmetry; mode-matching; twist symmetry

1. Introduction

Periodic structures have been extensively used to engineer the desired electromagnetic response in a wide range of devices; for instance, filters [1], frequency selective surfaces [2], antennas [3], absorbers [4], and lenses [5]. However, the usefulness of periodic structures is often limited by their inherent frequency dispersion, as well as their relatively low effective refractive index. Recently, it was demonstrated that the introduction of higher symmetries into a periodic structure can alleviate these limitations. A periodic structure is said to possess a higher-symmetric if it is invariant after a translation and an additional geometrical operation [6–9]. Consequently, the translational unit cell of a higher-symmetric structure can be divided into ξ sub-unit cells, where ξ is the (entire) order of the symmetry. The translational period of the higher-symmetric structure is then given by $p = \delta\xi$, where δ is the size (period) of the sub-unit cell. A generalized Floquet theorem was presented in [9], stating that the Bloch modes in a higher-symmetric structure are eigenmodes to both the translation operator of the unit cell, $\mathcal{T}_p$, and the compound operator applied to the sub-unit cell, $\mathcal{C}_\delta$. The most relevant result of this theorem is that it suffices to analyze the sub-unit cell of a higher-symmetric structure, which can significantly reduce the required computational resources. A direct consequence of the existence of ξ sub-unit cells within a unit cell is the absence of band gaps between the first ξ modes of the structure [10]. Mainly, two types of higher symmetries have been investigated for electromagnetic purposes: glide- and twist-symmetries. The additional geometrical operation in a glide and twist-symmetric structure is a mirroring in a plane and a rotation around an axis, respectively.

A glide symmetry is inherently of order $\xi = 2$, while a twist symmetry can have higher orders, $\xi \geq 2$, as happens for the four-fold twist-symmetric structure illustrated in Figure 1.

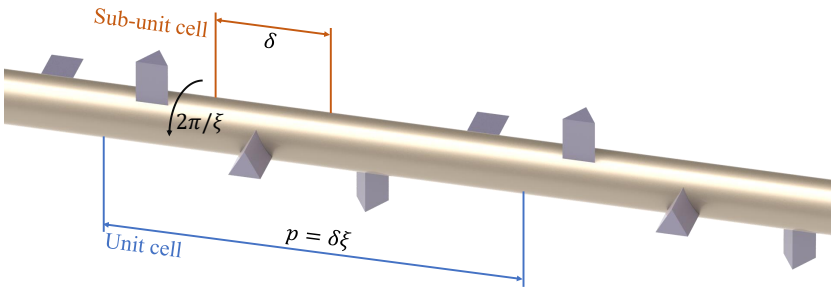

Figure 1. Illustration of a twist symmetry of order $\xi = 4$. The angle of the consecutive rotation here is $\pi/2$.

Recent studies of glide-symmetric structures have demonstrated the absence of the stop-band between the first and second modes [11,12]. Additionally, it has been demonstrated that glide-symmetric structures are less dispersive [12,13] and can provide a higher effective refractive index [13–16], effective permeability [17], and level of anisotropy [18], compared to their non-glide counterparts. These properties have been used to design planar lenses in [13,19–22]. Furthermore, while the stop-band between the first two modes is suppressed in glide-symmetric structures, a large stop-band exists at higher frequency [23–25]. This stop-band has been used to design low-cost gap waveguides [26] and filters [27] and to reduce the leakage between waveguide flanges [28,29]. These attractive properties have inspired the development of several semi-analytical methods for the analysis of glide-symmetric structures using circuit models [25,30,31], mode-matching [32–35], or the multimode transfer-matrix approach [36–38]. These methods provide a fast means of studying glide-symmetric structures and give insight into the physics of glide symmetry.

Similar properties have been demonstrated in twist-symmetric structures. However, since the order of the twist symmetry can be changed, an increased control of the electromagnetic response is enabled, compared to translational and glide-symmetric structures. For instance, the absence of stop-bands between the first ξ modes ($\xi \geq 2$) was demonstrated in [31,39–41]. Additionally, reduced frequency dispersion and an increased effective refractive index in twist-symmetric structures were demonstrated in [41]. These properties have been used to design twist-symmetric filters [40], phase-shifters [42], miniaturized helix antennas [43], lenses [44], and polarization filtering optical fibers [45]. Furthermore, in [42], a close relation between the twist symmetry and the existence of a broad pass-band was found in periodically loaded cylindrical waveguides. However, despite the numerous interesting properties of twist symmetries, to the authors' knowledge, only one work was aimed at providing physical insight into twist symmetries [46]. There, the multimode technique was employed to demonstrate that the coupling of the higher order modes is important to explain the different response in twist-symmetric structures with respect to non-twist-symmetric structures.

In the present work, a mode-matching formulation is presented for the dispersion analysis of periodically loaded coaxial transmission lines with twist symmetries. The formulation is validated using the commercial software CST Microwave Studio [47] and is used to provide new insights into the physics of twist symmetries. Specifically, we build on the study in [46], and we discuss in detail how the different higher order coaxial line modes (TMand TE) are linked to the order of the twist symmetry. Furthermore, it is demonstrated that the importance of the different coaxial line modes changes across the pass-band.

2. Problem Formulation

2.1. Description of the Analyzed Structures

The translational unit cells of the structures considered in this work are illustrated in Figure 2. They consist of a coaxial transmission line periodically loaded with infinitely thin sectorial metallic screens. The geometrical operation (in cylindrical coordinates) applied to the sub-unit cell describing the structure is given by:

$$S_\delta = \begin{cases} \rho & \rightarrow & \rho \\ \varphi & \rightarrow & \varphi + 2\pi/\xi \\ z & \rightarrow & z + \delta \end{cases} \tag{1}$$

where ρ, φ, and z are the cylindrical coordinates, and ξ is 2, 3, and 4 in Figure 2a–c, respectively. The structure in Figure 2d is the conventional periodic case. The radius of the inner and outer conductor of the coaxial is r_i and r_o, and the radius and opening angle of the screen are r_s and α. In [39], an alternative definition of the twist operator was used. However, the definition (1) ensures that the structures differ only by a mutual rotation between adjacent screens and is therefore used in the present work.

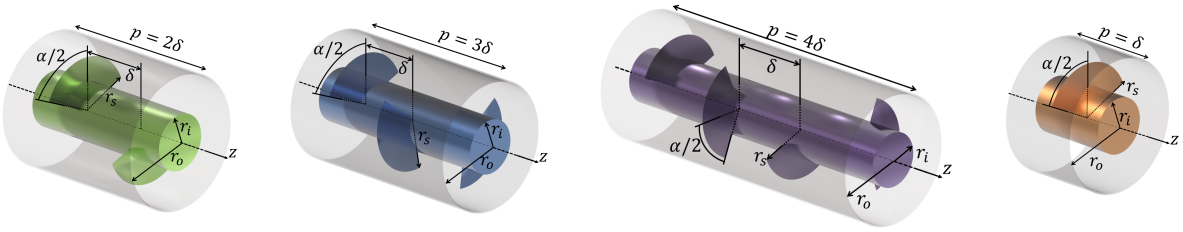

(**a**) (**b**) (**c**) (**d**)

Figure 2. Analyzed periodically loaded coaxial transmission lines: (**a**) 2-, (**b**) 3-, and (**c**) 4-fold twist-symmetric structures and (**d**) conventional periodic structure.

2.2. Enforcement of Symmetry and Periodicity

Due to the higher-symmetric in the structures, the generalized Floquet theorem [9] is used to analyze them. Therefore, only one sub-unit cell needs to be considered. The longitudinal and transversal cross-sectional views of the sub-unit cell are shown in Figure 3.

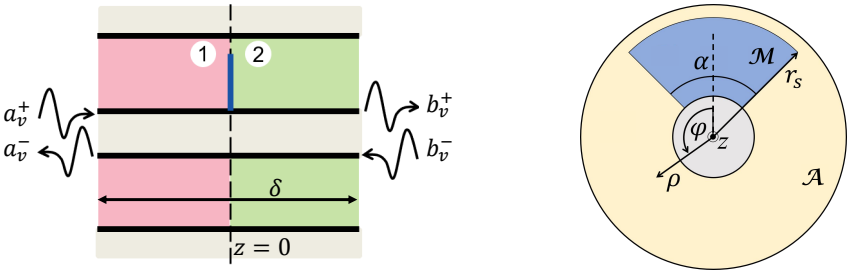

(**a**) (**b**)

Figure 3. Cross-sectional views of the sub-unit cell in the: (**a**) longitudinal plane and (**b**) transversal plane at the position of the screen.

It should be noted that, for the conventional periodic structure, the sub-unit cell is also the unit cell. The amplitudes of the coaxial line modes at Sides 1 and 2 of the sub-unit cell are referred to as $a_v^\pm$ and $b_v^\pm$, respectively. The subscript v is a combination of the angular and radial mode indices of a coaxial transmission line (m and n in the modal field expressions in Appendix A), and the superscript indicates the direction of propagation.

The Bloch modes supported by the structures are found through an eigenvalue problem that relates the coaxial line modes at the two sides of the sub-unit cell. The eigenvalue problem is constructed using the transfer matrix of the sub-unit cell, $\underline{\mathbf{T}}$, which relates the modes as:

$$\begin{bmatrix} \mathbf{b}^+ \\ \mathbf{b}^- \end{bmatrix} = \underline{\mathbf{T}} \begin{bmatrix} \mathbf{a}^+ \\ \mathbf{a}^- \end{bmatrix} . \tag{2}$$

The matrix $\underline{\mathbf{T}}$ can be decomposed into a transfer matrix for the screen, $\underline{\mathbf{T}}_\mathrm{s}$, and two transfer matrices for the coaxial line between two screens, $\underline{\mathbf{P}}_{\delta/2}$, as:

$$\underline{\mathbf{T}} = \underline{\mathbf{P}}_{\delta/2}\,\underline{\mathbf{T}}_\mathrm{s}\,\underline{\mathbf{P}}_{\delta/2} = \begin{bmatrix} \underline{\mathbf{P}}^+_{\delta/2} & \underline{\mathbf{0}} \\ \underline{\mathbf{0}} & \underline{\mathbf{P}}^-_{\delta/2} \end{bmatrix} \underline{\mathbf{T}}_\mathrm{s} \begin{bmatrix} \underline{\mathbf{P}}^+_{\delta/2} & \underline{\mathbf{0}} \\ \underline{\mathbf{0}} & \underline{\mathbf{P}}^-_{\delta/2} \end{bmatrix} \tag{3}$$

where $\underline{\mathbf{P}}^\pm_{\delta/2}$ are diagonal matrices with the entries $\mathrm{e}^{\mp \mathrm{j} k_{zu}\delta/2}$. It is noted here and explicitly shown in Section 2.3 that $\underline{\mathbf{T}}_\mathrm{s}$ is a block partitioned matrix with two row partitions and two column partitions. By applying the generalized Floquet boundary conditions to (2), we get:

$$\underline{\mathbf{P}}_{\delta/2}\,\underline{\mathbf{T}}_\mathrm{s}\,\underline{\mathbf{P}}_{\delta/2} \begin{bmatrix} \mathbf{a}^+ \\ \mathbf{a}^- \end{bmatrix} = \mathrm{e}^{-\mathrm{j}\beta\delta}\underline{\mathbf{Q}} \begin{bmatrix} \mathbf{a}^+ \\ \mathbf{a}^- \end{bmatrix} \tag{4}$$

where β is the sought phase constant and $\underline{\mathbf{Q}}$ is a block diagonal matrix with entries $\underline{\mathbf{q}}_v$ given in [46]:

$$\underline{\mathbf{q}}_v = \begin{cases} 1 & \text{for TEMor TM/TE with } m = 0 \\ \begin{bmatrix} \cos(2\pi m/\xi) & \sin(2\pi m/\xi) \\ -\sin(2\pi m/\xi) & \cos(2\pi m/\xi) \end{bmatrix} & \text{for TM/TE with } m \neq 0\,. \end{cases} \tag{5}$$

It should be noted that it is matrix $\underline{\mathbf{Q}}$ that introduces the twist symmetry in the formulation and that higher order modes with an angular variation are required to observe the effect of twist symmetry. Furthermore, for the TM and TE modes with $m = 0$, $\underline{\mathbf{q}}_v$ is a scalar, and for $\xi = 1$, $\underline{\mathbf{Q}}$ reduces to the identity matrix. The characteristic equation of the structure under study is found by solving the eigenvalue problem (4); namely, by searching for the values of β that satisfy:

$$\det[\underline{\mathbf{P}}_{\delta/2}\,\underline{\mathbf{T}}_\mathrm{s}\,\underline{\mathbf{P}}_{\delta/2} - \mathrm{e}^{-\mathrm{j}\beta\delta}\underline{\mathbf{Q}}] = 0\,. \tag{6}$$

2.3. Obtaining $\underline{\mathbf{T}}_\mathrm{s}$ Using the Mode-Matching Technique

The mode-matching technique is used to relate the coaxial line modes at the the two sides of the screen. The mode coefficients at the position of the screen are denoted $\tilde{\mathbf{a}}^\pm$ and $\tilde{\mathbf{b}}^\pm$ to distinguish them from the mode coefficients at the two ends of the sub-unit cell. Assuming and suppressing a time-dependence $\mathrm{e}^{\mathrm{j}\omega t}$, the transverse electric and magnetic fields at both sides of the screen can be expressed as:

$$\mathbf{E}_{1t}(\mathbf{r}) = \sum_{v=1}^{\infty} (\tilde{a}_v^+ \mathrm{e}^{-\mathrm{j}k_{zv}z} + \tilde{a}_v^- \mathrm{e}^{\mathrm{j}k_{zv}z})\,\mathbf{e}_v \tag{7}$$

$$\mathbf{H}_{1t}(\mathbf{r}) = \sum_{v=1}^{\infty} [(\tilde{a}_v^+ \mathrm{e}^{-\mathrm{j}k_{zv}z} - \tilde{a}_v^- \mathrm{e}^{\mathrm{j}k_{zv}z})\,\frac{1}{Z_v}\hat{\mathbf{z}} \times \mathbf{e}_v \tag{8}$$

$$\mathbf{E}_{2t}(\mathbf{r}) = \sum_{v=1}^{\infty} (\tilde{b}_v^+ \mathrm{e}^{-\mathrm{j}k_{zv}z} + \tilde{b}_v^- \mathrm{e}^{\mathrm{j}k_{zv}z})\,\mathbf{e}_v \tag{9}$$

$$\mathbf{H}_{2t}(\mathbf{r}) = \sum_{v=1}^{\infty} (\tilde{b}_v^+ \mathrm{e}^{-\mathrm{j}k_{zv}z} - \tilde{b}_v^- \mathrm{e}^{\mathrm{j}k_{zv}z})\,\frac{1}{Z_v}\hat{\mathbf{z}} \times \mathbf{e}_v \tag{10}$$

where the modal impedance, Z_v, is:

$$Z_v = \begin{cases} \eta & \text{TEM} \\ \dfrac{\eta k_{zv}}{k} & \text{TM} \\ \dfrac{\eta k}{k_{zv}} & \text{TE} \,. \end{cases} \tag{11}$$

Here, η and k are the free-space wave impedance and k_{zv} is the longitudinal wavenumber of the v-th mode of the guiding structure, with $\mathbf{e}_v$ being the transverse field of the v-th mode of the coaxial transmission line as detailed in the Appendix A [48]. It is worth noting here that the cos-/sin-degeneracy explicitly shown in the Appendix A gives rise to two modes with index v if $m \neq 0$. The transverse modal fields are orthonormalized over the cross-section $\mathcal{X} = \mathcal{A} + \mathcal{M}$ of the coaxial line with the inner product of modes u and v defined as the usual L^2 scalar product on the relevant domain:

$$\langle \mathbf{e}_u, \mathbf{e}_v \rangle_{\mathcal{X}} = \int_{\mathcal{X}} \mathbf{e}_u \cdot \mathbf{e}_v^* \, \mathrm{d}S = \langle \mathbf{e}_u, \mathbf{e}_v \rangle_{\mathcal{M}} + \langle \mathbf{e}_u, \mathbf{e}_v \rangle_{\mathcal{A}} = \delta_{uv} \tag{12}$$

where $\mathcal{M}$ and $\mathcal{A}$ correspond to the regions of the metallic screen and air aperture (indicated in Figure 3), δ_{uv} is the Kronecker delta, and * denotes the complex conjugate. A consequence of (12) is that the inner product can be equivalently performed either over the metallic screen or in the air aperture, which saves computational resources.

To relate the modes at the two sides of the screen, we apply the transverse field continuity conditions. The metallic screen is placed at $z = 0$, on which the transverse electric field must vanish because of its condition of being a perfect electric conductor. Therefore, at the metallic screen ($\boldsymbol{\rho} \in \mathcal{M}$), (7) and (9) become:

$$\sum_{v=1}^{\infty} (\tilde{a}_v^+ + \tilde{a}_v^-)\mathbf{e}_v = \sum_{v=1}^{\infty} (\tilde{b}_v^+ + \tilde{b}_v^-)\mathbf{e}_v = 0 \,, \qquad \boldsymbol{\rho} \in \mathcal{M} \,. \tag{13}$$

Furthermore, in the aperture ($\boldsymbol{\rho} \in \mathcal{A}$), the continuity of the transverse electric field gives:

$$\sum_{v=1}^{\infty} (\tilde{a}_v^+ + \tilde{a}_v^-)\mathbf{e}_v = \sum_{v=1}^{\infty} (\tilde{b}_v^+ + \tilde{b}_v^-)\mathbf{e}_v \,, \qquad \boldsymbol{\rho} \in \mathcal{A} \,. \tag{14}$$

Due to the orthogonality enforced in (12), the relationships (13) and (14) must hold term-wise, and thus:

$$\tilde{a}_v^+ + \tilde{a}_v^- = \tilde{b}_v^+ + \tilde{b}_v^- \,. \tag{15}$$

Similarly, from the continuity of $\mathbf{H}$ in the aperture ($\boldsymbol{\rho} \in \mathcal{A}$), we obtain:

$$\sum_{v=1}^{\infty} (\tilde{a}_v^+ - \tilde{a}_v^-)\frac{1}{Z_v}\mathbf{e}_v = \sum_{v=1}^{\infty} (\tilde{b}_v^+ - \tilde{b}_v^-)\frac{1}{Z_v}\mathbf{e}_v \,, \qquad \boldsymbol{\rho} \in \mathcal{A} \tag{16}$$

which, when combined with (13) and (15) in different ways, gives the following four relationships:

$$\sum_{v=1}^{\infty} \tilde{a}_v^- \mathbf{e}_v(\boldsymbol{\rho}) = -\sum_{v=1}^{\infty} \tilde{a}_v^+ \mathbf{e}_v(\boldsymbol{\rho}) \,, \qquad \boldsymbol{\rho} \in \mathcal{M} \tag{17}$$

$$\sum_{v=1}^{\infty} \tilde{a}_v^- \frac{1}{Z_v}\mathbf{e}_v(\boldsymbol{\rho}) = \sum_{v=1}^{\infty} \tilde{b}_v^- \frac{1}{Z_v}\mathbf{e}_v(\boldsymbol{\rho}) \,, \qquad \boldsymbol{\rho} \in \mathcal{A} \tag{18}$$

$$\sum_{v=1}^{\infty} \tilde{b}_v^+ \mathbf{e}_v(\boldsymbol{\rho}) = -\sum_{v=1}^{\infty} \tilde{b}_v^- \mathbf{e}_v(\boldsymbol{\rho}) \,, \qquad \boldsymbol{\rho} \in \mathcal{M} \tag{19}$$

$$\sum_{v=1}^{\infty} \tilde{b}_v^+ \frac{1}{Z_v}\mathbf{e}_v(\boldsymbol{\rho}) = \sum_{v=1}^{\infty} \tilde{a}_v^+ \frac{1}{Z_v}\mathbf{e}_v(\boldsymbol{\rho}) \,, \qquad \boldsymbol{\rho} \in \mathcal{A} \,. \tag{20}$$

If the inner products of $\mathbf{e}_u$ with the relationships (17)–(20) are linearly combined as $Z_u^{-1}\langle \mathbf{e}_u, (17)\rangle_{\mathcal{M}} + \langle \mathbf{e}_u, (18)\rangle_{\mathcal{A}}$ and $Z_u^{-1}\langle \mathbf{e}_u, (19)\rangle_{\mathcal{M}} + \langle \mathbf{e}_u, (20)\rangle_{\mathcal{A}}$, we obtain:

$$\sum_{v=1}^{\infty}\left[\delta_{uv} + \left(\frac{Z_u}{Z_v} - 1\right)\langle \mathbf{e}_u, \mathbf{e}_v\rangle_{\mathcal{A}}\right]\tilde{a}_v^- = \sum_{v=1}^{\infty}\left[\left(\langle \mathbf{e}_u, \mathbf{e}_v\rangle_{\mathcal{A}} - \delta_{uv}\right)\tilde{a}_v^+ + \frac{Z_u}{Z_v}\langle \mathbf{e}_u, \mathbf{e}_v\rangle_{\mathcal{A}}\,\tilde{b}_v^-\right] \tag{21}$$

and:

$$\sum_{v=1}^{\infty}\left[\delta_{uv} + \left(\frac{Z_u}{Z_v} - 1\right)\langle \mathbf{e}_u, \mathbf{e}_v\rangle_{\mathcal{A}}\right]\tilde{b}_v^+ = \sum_{v=1}^{\infty}\left[\left(\langle \mathbf{e}_u, \mathbf{e}_v\rangle_{\mathcal{A}} - \delta_{uv}\right)\tilde{b}_v^- + \frac{Z_u}{Z_v}\langle \mathbf{e}_u, \mathbf{e}_v\rangle_{\mathcal{A}}\,\tilde{a}_v^+\right] \tag{22}$$

where the inner products over the metallic screen, $\mathcal{M}$, have been substituted with inner products over the air aperture, $\mathcal{A}$, using (12). Equations (21) and (22) relate the coaxial mode amplitudes at the two sides of the screen and can be expressed in matrix form as:

$$\underline{\mathbf{\Pi}}\tilde{\mathbf{a}}^- = \underline{\mathbf{\Delta}}\tilde{\mathbf{a}}^+ + \underline{\mathbf{\Omega}}\tilde{\mathbf{b}}^- \tag{23}$$

$$\underline{\mathbf{\Pi}}\tilde{\mathbf{b}}^+ = \underline{\mathbf{\Delta}}\tilde{\mathbf{b}}^- + \underline{\mathbf{\Omega}}\tilde{\mathbf{a}}^+ \tag{24}$$

where the elements of the matrices are:

$$\Pi_{uv} = \delta_{uv} + \left(\frac{Z_u}{Z_v} - 1\right)\langle \mathbf{e}_u, \mathbf{e}_v\rangle_{\mathcal{A}} \tag{25}$$

$$\Delta_{uv} = \langle \mathbf{e}_u, \mathbf{e}_v\rangle_{\mathcal{A}} - \delta_{uv} \tag{26}$$

$$\Omega_{uv} = \left(\frac{Z_u}{Z_v} - 1\right)\langle \mathbf{e}_u, \mathbf{e}_v\rangle_{\mathcal{A}}\ . \tag{27}$$

By rearranging (23) and (24), we get:

$$\begin{bmatrix}\tilde{\mathbf{b}}^+ \\ \tilde{\mathbf{b}}^-\end{bmatrix} = \underline{\mathbf{T}}_s\begin{bmatrix}\tilde{\mathbf{a}}^+ \\ \tilde{\mathbf{a}}^-\end{bmatrix} \tag{28}$$

where the transfer matrix of the screen is:

$$\underline{\mathbf{T}}_s = \begin{bmatrix}\underline{\mathbf{\Pi}}^{-1}\underline{\mathbf{\Omega}} - \underline{\mathbf{\Pi}}^{-1}\underline{\mathbf{\Delta}}\underline{\mathbf{\Omega}}^{-1}\underline{\mathbf{\Delta}} & \underline{\mathbf{\Pi}}^{-1}\underline{\mathbf{\Delta}}\underline{\mathbf{\Omega}}^{-1}\underline{\mathbf{\Pi}} \\ -\underline{\mathbf{\Omega}}^{-1}\underline{\mathbf{\Delta}} & \underline{\mathbf{\Omega}}^{-1}\underline{\mathbf{\Pi}}\end{bmatrix}\ . \tag{29}$$

The Bloch modes of the structure are found by inserting (29) into (6).

3. Results

The mode-matching formulation was implemented in MATLAB [49] and used to study the dispersion diagrams of the structures in Figure 2. The geometrical dimensions of the structure are $r_i = 2\,\text{mm}$, $r_o = 4.7\,\text{mm}$, $r_s = 4.7\,\text{mm}$, $\alpha = 180°$, and $\delta = 6\,\text{mm}$. With these dimensions, the screen connects the inner and outer conductors of the coaxial lines, and as a result, the first mode has a cut-off frequency. This configuration is chosen so that the mode-matching formulation converges quickly: good convergence is achieved by only including higher order modes with $n = 1$. The convergence of the numerical result is evaluated by comparing the root-mean-squared deviation of the obtained samples of β for different numbers of coaxial line modes included in the computation. The convergence is deemed sufficient if the result deviates less than 1% when including an additional coaxial line mode. In the studied structures, 1 TEM, 17 TM, and 7 TE modes were found to ensure convergence.

The dispersion diagrams of the analyzed twist-symmetric structures are plotted in Figure 4. The results obtained using the mode-matching formulation agree well with the ones computed using the Eigenmode Solver of CST. The curves in Figure 4 show that, with the definition of the twist operator

in (1), the dispersion diagrams converge to that of the conventional periodic structure as the order of the symmetry increases. This observation is supported by the fact that the conventional periodic structure is equivalent to an ∞-fold twist-symmetric structure with the present definition of the twist operator. For alternative definitions of the twist operator (as the one used in [39]), this is not necessarily the case.

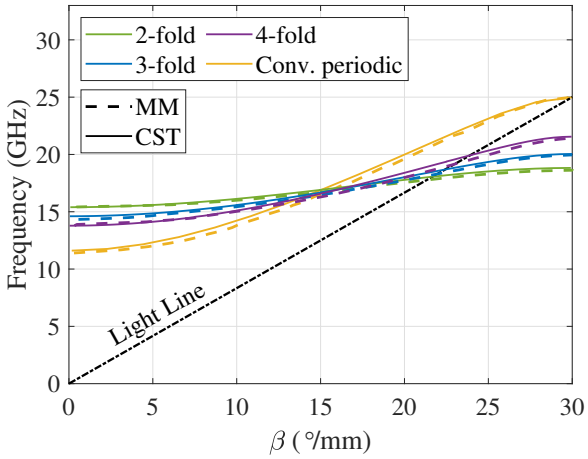

Figure 4. Comparison of the obtained dispersion curves for the studied structures between the mode-matching formulation and CST. The dimensions are: $r_i = 2\,\text{mm}$, $r_o = 4.7\,\text{mm}$, $r_s = 4.7\,\text{mm}$, $\alpha = 180°$, and $\delta = 6\,\text{mm}$. In the mode-matching formulation, 1 TEM, 17 TM, and 7 TEmodes are included.

A valuable insight that the mode-matching analysis directly provides comes from the analysis of the magnitudes of the different coaxial cable modes. This analysis gives us useful information about the field characteristics, as well as its most convenient way of being excited. Thus, the magnitudes of the coaxial cable mode coefficients for three values of the phase constant (β) are presented in Figure 5. The mode coefficients are normalized so that $|\mathbf{a}| = 1$.

A first interesting observation in Figure 5 is that the magnitude of the TEM mode does not vary too much in the three cases shown in the figure. It can also be observed that the degrees of excitation of the TEM and the TE_{11} modes are similar and greater than the one of the TM modes. However, the data in Figure 5a show that there is a significant variation of the magnitudes of the TM modes as the symmetry order (ξ) of the analyzed structures changes. This latter fact can be explained taking into account that the neighboring screens form lengthwise capacitors for the z-directed electric fields of these TM modes. The magnitudes of the TM modes are then expected to depend on the degree of overlap between consecutive metallic plates; namely, with the value of ξ. A similar trend to that in Figure 4 is observed here, as the mode magnitudes in the twist-symmetric structures converge to those of the conventional periodic structure as ξ increases. Figure 5a also shows that the magnitude of the TE_{11} increases as the symmetry order decreases. This is consistent with the fact that the cutoff frequency of the TE_{11} mode is ∼15 GHz, and the dispersion curves in Figure 4 show that, for $\beta = 6\,°/\text{mm}$, the smaller ξ is, the closer the corresponding frequency appears to that cutoff frequency. In the cases shown in Figure 5b,c, since the corresponding modal solutions appear at frequencies above the TE_{11} cutoff frequency, a significant decrease in the relative importance of the TM modes with respect to the TE_{11} mode can be observed. This trend is further illustrated in Figure 6, where the mode magnitudes for the TM_{11} and TE_{11} modes are plotted vs. the phase constant (only the degenerate mode with the largest magnitude is plotted). In these figures, each curve contain 100 samples of the mode coefficients in the pass-band, and the band edges are omitted due to instabilities in the numerical result. It is observed that when the TE_{11} mode begins to propagate, there is an apparent prevalence of this mode with respect to TM_{11}.

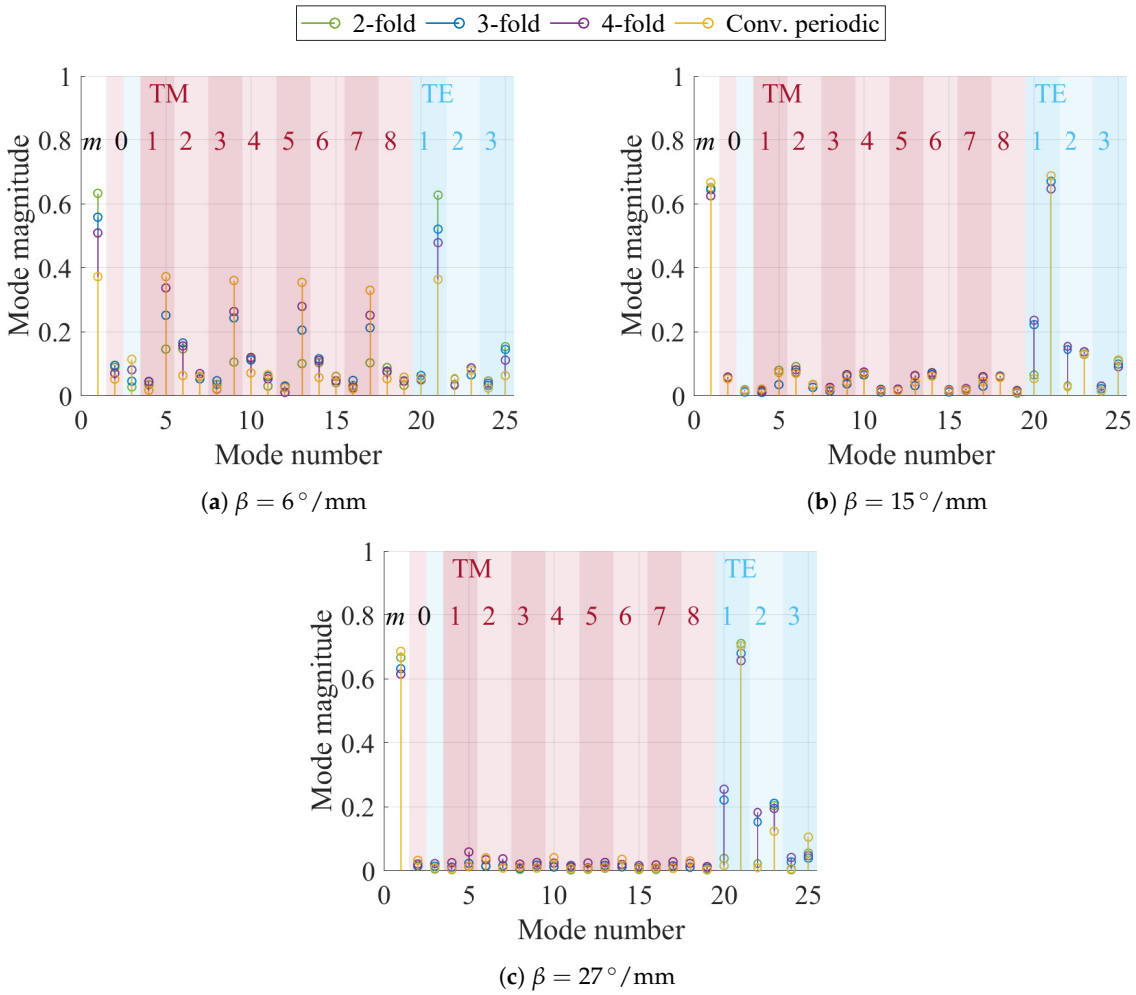

(**a**) $\beta = 6\,^\circ/\text{mm}$ (**b**) $\beta = 15\,^\circ/\text{mm}$

(**c**) $\beta = 27\,^\circ/\text{mm}$

Figure 5. Magnitudes of the mode coefficients for different phases: (**a**) $\beta = 6\,^\circ/\text{mm}$, (**b**) $\beta = 15\,^\circ/\text{mm}$, and (**c**) $\beta = 27\,^\circ/\text{mm}$. The dimensions are the same as in Figure 4.

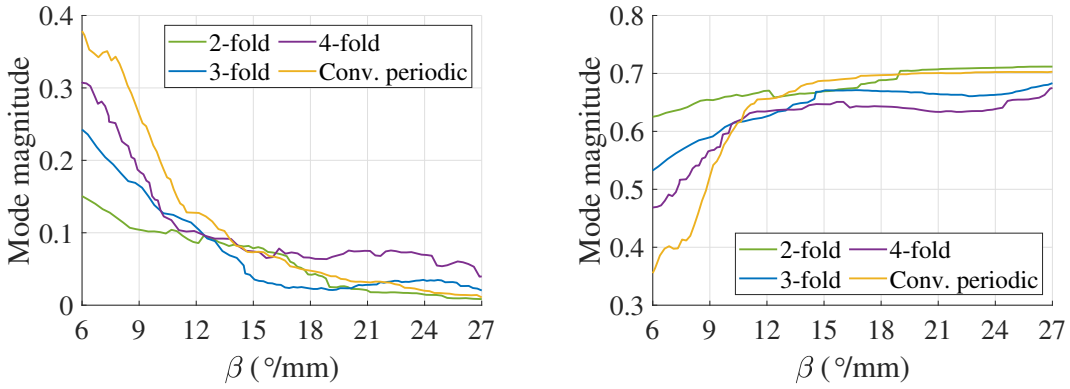

(**a**) TM_{11} mode (**b**) TE_{11} mode

Figure 6. Magnitudes of the mode coefficients of the TM_{11} and TE_{11} modes. The dimensions and number of modes are the same as in Figure 4.

For $\beta \gtrsim 14\,^\circ/\text{mm}$, it can be noticed in Figure 4 that the propagation frequencies increase with the symmetry order, which is opposed to what happens in the range $\beta \lesssim 14\,^\circ/\text{mm}$. However, Figure 5b,c shows that the magnitude of the mode coefficients is similar in all the analyzed structures. To understand the difference in the response for $\beta \gtrsim 14\,^\circ/\text{mm}$, a more detailed analysis should be carried out on the impact of the relevant modes at these frequencies (TEM and TE_{11}). In Figure 7,

the phase of the mode coefficients vs. β for the TEM and TE_{11} modes is presented. It is observed that the phase of the TEM mode coefficient is similar in all the analyzed structures, as illustrated in Figure 7a. Furthermore, for $\beta \gtrsim 14\,^{\circ}/\text{mm}$, it is noted that the phases of the mode coefficient for the TEM and TE_{11} are similar in the conventional periodic structure. However, as subsequent screens are rotated, the phase of the TE_{11} mode coefficient changes, as illustrated in Figure 7b. In other words, the impact of the TE_{11} mode varies with ξ, and the difference is particularly large between the three twisted structures and the conventional periodic structure. This confirms the difference in the dispersion curves observed in Figure 4.

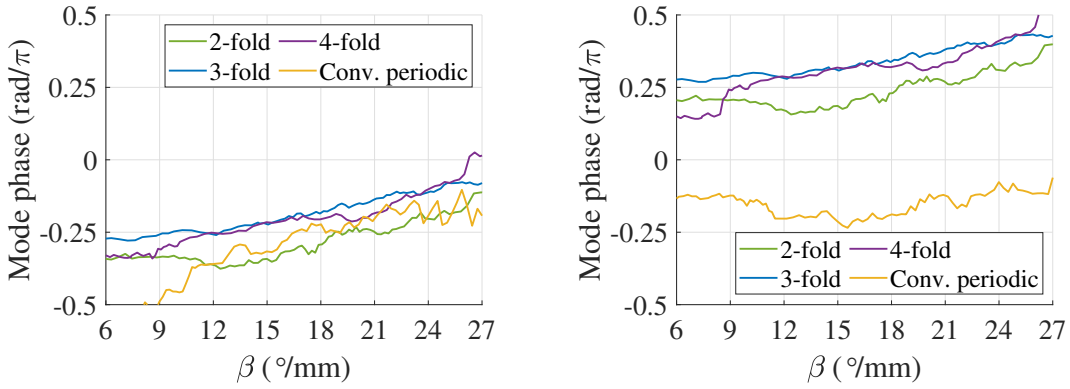

(**a**) TEM mode (**b**) TE_{11} mode

Figure 7. Phases of the mode coefficients of the: (**a**) TEM and (**b**) TE_{11} modes. In this simulation, the dimensions and number of modes are the same as in Figure 4.

4. Conclusions

Twist symmetry has recently been demonstrated to provide attractive properties for the design of electromagnetic devices. In this article, we analyze the dispersive properties of twist-symmetric transmission lines using the mode-matching technique. The analyzed structures consist of coaxial lines periodically loaded with infinitely thin sectorial metallic screens. The employed mode-matching formulation is presented, and the results agree well with the results obtained using commercial software. The formulation is used to provide physical insight into the phenomenon of twist symmetries. Specifically, the importance of the higher order modes on the dispersion properties of twist-symmetric structures is demonstrated, and it is shown that that the relevant higher order modes impact the propagation characteristics differently depending on the symmetry order. This insight is valuable for the design of filters [40], phase-shifters [42], antennas [43], lenses [44], and optical fibers [45].

Author Contributions: Conceptualization, G.V. and O.Q.-T.; methodology, G.V., M.N., and O.Q.-T.; software, O.Z.; formal analysis, O.Z., G.V., F.M., F.G., M.N., and O.Q.-T.; writing, original draft preparation, O.Z.; writing, review and editing, O.Z., G.V., F.M., F.G., M.N., and O.Q.-T.; visualization, O.Z.; supervision, G.V., F.M., F.G., M.N., and O.Q.-T. All authors have read and agreed to the published version of the manuscript.

Funding: This research was funded by Vinnova project High-5 Grant Number 2018-01522, Stiftelsen Åforsk project H-Materials Grant Number 18-302, the French National Research Agency Grant Number ANR-16-CE24-0030, and the Spanish Government Salvador de Madariaga fellowship (Number PRX19/00025) and Project Number TEC2017-84724-P.This article is based upon work from COST Action SyMat CA18223, supported by COST (European Cooperation in Science and Technology), www.cost.eu/.

Conflicts of Interest: The authors declare no conflict of interest.

Appendix A

In (7)–(10), the transverse modal field of the coaxial transmission line is given by:

$$\mathbf{e}_v = \mathbf{e}_{v(m,n)}(\boldsymbol{\rho}) = \mathbf{e}^{\rho}_{mn}(\boldsymbol{\rho}) + \mathbf{e}^{\varphi}_{mn}(\boldsymbol{\rho}) \tag{A1}$$

with:

$$\mathbf{e}^{\rho}_{mn}(\boldsymbol{\rho}) = \begin{cases} \dfrac{1}{\sqrt{2\pi \ln(r_o/r_i)}} \dfrac{1}{\rho} \hat{\boldsymbol{\rho}} & \text{TEM} \\ -\dfrac{\mathrm{j}k_{zmn}}{k_{tmn}} E_{zmn} \left[J'_m(k_{tmn}\rho) Y_m(k_{tmn} r_i) - J_m(k_{tmn} r_i) Y'_m(k_{tmn}\rho) \right] \begin{pmatrix} \cos(m\varphi) \\ \sin(m\varphi) \end{pmatrix} \hat{\boldsymbol{\rho}} & \text{TM} \\ -\dfrac{\mathrm{j}k\eta}{k^2_{tmn}} H_{zmn} \dfrac{m}{\rho} \left[J_m(k_{tmn}\rho) Y'_m(k_{tmn} r_i) - J'_m(k_{tmn} r_i) Y_m(k_{tmn}\rho) \right] \begin{pmatrix} -\sin(m\varphi) \\ \cos(m\varphi) \end{pmatrix} \hat{\boldsymbol{\rho}} & \text{TE} \end{cases} \tag{A2}$$

and:

$$\mathbf{e}^{\varphi}_{mn}(\boldsymbol{\rho}) = \begin{cases} 0 & \text{TEM} \\ -\dfrac{\mathrm{j}k_{zmn}}{k^2_{tmn}} E_{zmn} \dfrac{m}{\rho} \left[J_m(k_{tmn}\rho) Y_m(k_{tmn} r_i) - J_m(k_{tmn} r_i) Y_m(k_{tmn}\rho) \right] \begin{pmatrix} -\sin(m\varphi) \\ \cos(m\varphi) \end{pmatrix} \hat{\boldsymbol{\varphi}} & \text{TM} \\ \dfrac{\mathrm{j}k\eta}{k_{tmn}} H_{zmn} \left[J'_m(k_{tmn}\rho) Y'_m(k_{tmn} r_i) - J'_m(k_{tmn} r_i) Y'_m(k_{tmn}\rho) \right] \begin{pmatrix} \cos(m\varphi) \\ \sin(m\varphi) \end{pmatrix} \hat{\boldsymbol{\varphi}} & \text{TE} \end{cases} \tag{A3}$$

where $J_m(\cdot)$ and $Y_m(\cdot)$ are the Bessel functions of the first and second kind and $k_{tmn} = k_{tv}$ and $k_{zmn} = k_{zv}$ are the transverse and longitudinal wavenumbers of the guiding structure [48]. The coefficients E_{zmn} and H_{zmn} are found by orthonormalizing the modal fields over the cross-section of the coaxial line.

References

1. Sharp, E.D. A High-Power Wide-Band Waffle-Iron Filter. *IEEE Trans. Microw. Theory Tech.* **1963**, *11*, 111–116. [CrossRef]
2. Pous, R.; Pozar, D.M. A frequency-selective surface using aperture-coupled microstrip patches. *IEEE Trans. Antennas Propag.* **1991**, *39*, 1763–1769. [CrossRef]
3. Faenzi, M.; Minatti, G.; González-Ovejero, D.; Caminita, F.; Martini, E.; Della Giovampaola, C.; Maci, S. Metasurface Antennas: New Models, Applications and Realizations. *Sci. Rep.* **2019**, *9*, 10178. [CrossRef] [PubMed]
4. Liu, X.; Fan, K.; Shadrivov, I.V.; Padilla, W.J. Experimental realization of a terahertz all-dielectric metasurface absorber. *Opt. Express* **2017**, *25*, 191–201. [CrossRef] [PubMed]
5. Bosiljevac, M.; Casaletti, M.; Caminita, F.; Sipus, Z.; Maci, S. Non-Uniform Metasurface Luneburg Lens Antenna Design. *IEEE Trans. Antennas Propag.* **2012**, *60*, 4065–4073. [CrossRef]
6. Crepeau, P.J.; McIsaac, P.R. Consequences of Symmetry in Periodic Structures. *Proc. IEEE* **1963**, *52*, 33–43. [CrossRef]
7. Mittra, R.; Laxpati, S. Propagation in a Wave Guide with Glide Reflection Symmetry. *Can. J. Phys.* **1965**, *43*, 353–372. [CrossRef]
8. Kieburtz, R.; Impagliazzo, J. Multimode Propagation on Radiating Traveling-Wave Structures with Glide-Symmetric Excitation. *IEEE Trans. Antennas Propag.* **1970**, *18*, 3–7. [CrossRef]
9. Hessel, A.; Chen, M.H.; Li, R.C.M.; Oliner, A.A. Propagation in Periodically Loaded Waveguides with Higher Symmetries. *Proc. IEEE* **1973**, *61*, 183–195. [CrossRef]
10. Ghasemifard, F. Periodic Structures with Higher Symmetries: Analysis and Applications. Ph.D. Thesis, KTH Royal Institute of Technology, Stockholm, Sweden, 2018.
11. Quesada, R.; Martín-Cano, D.; García-Vidal, F.; Bravo-Abad, J. Deep-Subwavelength Negative-Index Waveguiding Enabled By Coupled Conformal Surface Plasmons. *Opt. Lett.* **2014**, *39*, 2990–2993. [CrossRef]
12. Quevedo-Teruel, O.; Ebrahimpouri, M.; Ng Mou Kehn, M. Ultrawideband Metasurface Lenses Based on Off-Shifted Opposite Layers. *IEEE Antennas Wirel. Propag. Lett.* **2016**, *15*, 484–487. [CrossRef]
13. Arnberg, P.; Barreira Petersson, O.; Zetterstrom, O.; Ghasemifard, F.; Quevedo-Teruel, O. High Refractive Index Electromagnetic Devices in Printed Technology Based on Glide-Symmetric Periodic Structures. *Appl. Sci.* **2020**, *10*, 3216. [CrossRef]
14. Chang, T.; Kim, J.U.; Kang, S.K.; Kim, H.; Kim, D.K.; Lee, Y.H.; Shin, J. Broadband giant-refractive-index material based on mesoscopic space-filling curves. *Nat. Commun.* **2016**, *7*, 12661. [CrossRef] [PubMed]

15. Cavallo, D.; Felita, C. Analytical formulas for artificial dielectrics with nonaligned layers. *IEEE Trans. Antennas Propag.* **2017**, *65*, 5303–5311. [CrossRef]
16. Cavallo, D. Dissipation Losses in Artificial Dielectric Layers. *IEEE Trans. Antennas Propag.* **2018**, *66*, 7460–7465. [CrossRef]
17. Ebrahimpouri, M.; Herran, L.F.; Quevedo-Teruel, O. Wide-Angle Impedance Matching Using Glide-Symmetric Metasurfaces. *IEEE Microw. Wirel. Compon. Lett.* **2020**, *30*, 8–11. [CrossRef]
18. Ebrahimpouri, M.; Quevedo-Teruel, O. Ultrawideband Anisotropic Glide-Symmetric Metasurfaces. *IEEE Antennas Wirel. Propag. Lett.* **2019**, *18*, 1547–1551. [CrossRef]
19. Quevedo-Teruel, O.; Miao, J.; Mattsson, M.; Algaba-Brazalez, A.; Johansson, M.; Manholm, L. Glide-Symmetric Fully Metallic Luneburg Lens for 5G Communications at Ka-Band. *IEEE Antennas Wirel. Propag. Lett.* **2018**, *17*, 1588–1592. [CrossRef]
20. Fan, F.; Cai, M.; Zhang, J.; Yan, Z.; Wu, J. Wideband Low-Profile Luneburg Lens Based on a Glide-Symmetric Metasurface. *IEEE Access* **2020**, *8*, 85698–85705. [CrossRef]
21. Alex-Amor, A.; Ghasemifard, F.; Valerio, G.; Ebrahimpouri, M.; Padilla, P.; Fernandez-Gonzalez, J.M.; Quevedo-Teruel, O. Glide-Symmetric Metallic Structures with Elliptical Holes for Lens Compression. *IEEE Trans. Microw. Theory Techn.* **2020**. [CrossRef]
22. Bantavis, P.; Gonzalez, C.G.; Sauleau, R.; Goussetis, G.; Tubau, S.; Legay, H. Broadband graded index Gutman lens with a wide field of view utilizing artificial dielectrics: A design methodology. *Opt. Express* **2020**, *28*, 14648–14661. [CrossRef] [PubMed]
23. Ebrahimpouri, M.; Quevedo-Teruel, O.; Rajo-Iglesias, E. Design Guidelines for Gap Waveguide Technology Based on Glide-Symmetric Holey Structures. *IEEE Microw. Wirel. Compon. Lett.* **2017**, *27*, 542–544. [CrossRef]
24. Ebrahimpouri, M. High Frequency Microwave and Antenna Devices Based on Transformation Optics and Glide-Symmetric Metasurfaces. Ph.D. Thesis, KTH Royal Institute of Technology, Stockholm, Sweden, 2019.
25. Mouris, B.A.; Fernández-Prieto, A.; Thobaben, R.; Martel, J.; Mesa, F.; Quevedo-Teruel, O. On the Increment of the Bandwidth of Mushroom-Type EBG Structures With Glide Symmetry. *IEEE Trans. Microw. Theory Tech.* **2020**, *68*, 1365–1375. [CrossRef]
26. Ebrahimpouri, M.; Rajo-Iglesias, E.; Sipus, Z.; Quevedo-Teruel, O. Cost-Effective Gap Waveguide Technology Based on Glide-Symmetric Holey EBG Structures. *IEEE Trans. Microw. Theory Tech.* **2018**, *66*, 927–934. [CrossRef]
27. Monje-Real, A.; Fonseca, N.J.G.; Zetterstrom, O.; Pucci, E.; Quevedo-Teruel, O. Holey Glide-Symmetric Filters for 5G at Millimeter-Wave Frequencies. *IEEE Microw. Wirel. Compon. Lett.* **2020**, *30*, 31–34. [CrossRef]
28. Ebrahimpouri, M.; Brazalez, A.A.; Manholm, L.; Quevedo-Teruel, O. Using Glide-Symmetric Holes to Reduce Leakage between Waveguide Flanges. *IEEE Microw. Wirel. Compon. Lett.* **2018**, *28*, 473–475. [CrossRef]
29. He, Z.; An, S.; Liu, J.; Jin, C. Variable High Precision Wide D-band Phase Shifter. *IEEE Access* **2020**, *8*, 140438–140444. [CrossRef]
30. Valerio, G.; Sipus, Z.; Grbic, A.; Quevedo-Teruel, O. Accurate Equivalent-Circuit Descriptions of Thin Glide-Symmetric Corrugated Metasurfaces. *IEEE Trans. Antennas Propag.* **2017**, *65*, 2695–2700. [CrossRef]
31. Chen, Q.; Ghasemifard, F.; Valerio, G.; Quevedo-Teruel, O. Modeling and Dispersion Analysis of Coaxial Lines With Higher Symmetries. *IEEE Trans. Microw. Theory Tech.* **2018**, *66*, 1–8. [CrossRef]
32. Valerio, G.; Ghasemifard, F.; Sipus, Z.; Quevedo-Teruel, O. Glide-Symmetric All-Metal Holey Metasurfaces for Low-Dispersive Artificial Materials: Modeling and Properties. *IEEE Trans. Microw. Theory Tech.* **2018**, *66*, 1–14. [CrossRef]
33. Ghasemifard, F.; Norgren, M.; Quevedo-Teruel, O. Dispersion Analysis of 2-D Glide-Symmetric Corrugated Metasurfaces Using Mode-Matching Technique. *IEEE Microw. Wirel. Compon. Lett.* **2018**, *28*, 1–3. [CrossRef]
34. Ghasemifard, F.; Norgren, M.; Quevedo-Teruel, O.; Valerio, G. Analyzing Glide-Symmetric Holey Metasurfaces Using a Generalized Floquet Theorem. *IEEE Access* **2018**, *6*, 71743–71750. [CrossRef]
35. Alex-Amor, A.; Valerio, G.; Ghasemifard, F.; Mesa, F.; Padilla, P.; Fernandez-Gonzalez, J.M.; Quevedo-Teruel, O. Wave Propagation in Periodic Metallic Structures with Equilateral Triangular Holes. *Appl. Sci.* **2020**, *10*, 1600. [CrossRef]
36. Mesa, F.; Rodríguez-Berral, R.; Medina, F. On the computation of the dispersion diagram of symmetric one-dimensionally periodic structures. *Symmetry* **2018**, *10*, 307. [CrossRef]

37. Bagheriasl, M.; Quevedo-Teruel, O.; Valerio, G. Bloch Analysis of Artificial Lines and Surfaces Exhibiting Glide Symmetry. *IEEE Trans. Microw. Theory Tech.* **2019**, *67*, 2618–2628. [CrossRef]
38. Mesa, F.; Valerio, G.; Rodríguez-Berral, R.; Quevedo-Teruel, O. Simulation-Assisted Efficient Computation of the Dispersion Diagram of Periodic Structures. *IEEE Antennas Propag. Mag.* **2020**, 1–11, to be published.
39. Dahlberg, O.; Mitchell-Thomas, R.; Quevedo-Teruel, O. Reducing the Dispersion of Periodic Structures with Twist and Polar Glide Symmetries. *Sci. Rep.* **2017**, *7*, 10136. [CrossRef]
40. Ghasemifard, F.; Norgren, M.; Quevedo-Teruel, O. Twist and Polar Glide Symmetries: An Additional Degree of Freedom to Control The Propagation Characteristics of Periodic Structures. *Sci. Rep.* **2018**, *8*, 11266. [CrossRef]
41. Dahlberg, O.; Ghasemifard, F.; Valerio, G.; Quevedo-Teruel, O. Propagation characteristics of periodic structures possessing twist and polar glide symmetries. *EPJ Appl. Metamat.* **2019**, *6*,. 14 [CrossRef]
42. Quevedo-Teruel, O.; Dahlberg, O.; Valerio, G. Propagation in Waveguides with Transversal Twist-Symmetric Holey Metallic Plates. *IEEE Microw. Wirel. Compon. Lett.* **2018**, *28*, 1–3. [CrossRef]
43. Palomares-Caballero, A.; Padilla, P.; Alex-Amor, A.; Valenzuela-Valdes, J.; Quevedo-Teruel, O. Twist and glide symmetries for helix antenna design and miniaturization. *Symmetry* **2019**, *11*, 349. [CrossRef]
44. Dahlberg, O.; Valerio, G.; Quevedo-Teruel, O. Fully Metallic Flat Lens Based on Locally Twist-Symmetric Array of Complementary Split-Ring Resonators. *Symmetry* **2019**, *11*, 581. [CrossRef]
45. Kopp, V.I.; Churikov, V.M.; Singer, J.; Chao, N.; Neugroschl, D.; Genack, A.Z. Chiral Fiber Gratings. *Science* **2004**, *305*, 74–75. [CrossRef] [PubMed]
46. Bagheriasl, M.; Valerio, G. Bloch Analysis of Electromagnetic Waves in Twist-Symmetric Lines. *Symmetry* **2019**, *11*, 620. [CrossRef]
47. CST Microwave Studio, Version 2019. Availsble online: http://www.cst.com/ (accessed on 19 July 2020).
48. Pozar, D.M. *Microwave Engineering*; John Wiley & Sons: Hoboken, NJ, USA, 1998; pp. 163–170.
49. Matlab, Version 2020. Available online: https://se.mathworks.com/ (accessed on 19 July 2020).